Dynamics of highly excited barium atoms deposited on large argon clusters. I. General trends

A. Masson,[1] L. Poisson,[1] M.-A. Gaveau,[1] B. Soep,[1] J.-M. Mestdagh,[1,a)] V. Mazet,[2] and F. Spiegelman[3]

[1]*Laboratoire Francis Perrin, CNRS-URA 2453, CEA, IRAMIS, Service des Photons Atomes et Molécules, F-91191 Gif-sur-Yvette Cedex, France*
[2]*LSIIT (UMR 7005 University of Strasbourg-CNRS), Boulevard Sébastien Brant, BP 10413, 67412 Illkirch Cedex, France*
[3]*Laboratoire de Chimie et Physique Quantiques, IRSAMC, Université de Toulouse, UPS and CNRS, 118 Route de Narbonne, F-31062 Toulouse Cedex, France*

$Ba(Ar)_{\approx 750}$ clusters were generated by associating the supersonic expansion and the pick-up techniques. A femtosecond pump (266.3 nm)-probe (792 or 399.2 nm) experiment was performed to document the dynamics of electronically excited barium within the very multidimensional environment of the argon cluster. Barium was excited in the vicinity of the $6s9p$ ^1P state and probed by ionization. The velocity imaging technique was used to monitor the energy distribution of photoelectrons and photoions as a function of the delay time between the pump and the probe pulses. A complex dynamics was revealed, which can be interpreted as a sequence/superposition of elementary processes, one of which is the ejection of barium out of the cluster. The latter has an efficiency, which starts increasing 5 ps after the pump pulse, the largest ejection probability being at 10 ps. The ejection process lasts at a very long time, up to 60 ps. A competing process is the partial solvation of barium in low lying electronic states. Both processes are preceded by a complex electronic relaxation, which is not fully unraveled here, the present paper being the first one in a series. © *2010 American Institute of Physics.* [doi:10.1063/1.3464489]

I. INTRODUCTION

The nonadiabatic coupling of electronic and nuclear motions has attracted attention since the early age of quantum mechanics. From a theoretical point of view, two limiting situations were considered in early works, namely, (i) when a single degree of freedom is involved and a limited number of energy states are coupled (e.g. the approach of Landau[1] and Zener[2]) and (ii) when the excited system is immersed in a quasicontinuous bath of perturbing levels.[3] Intermediate and more realistic situations are very challenging, and since then, the field of nonadiabatic dynamics has significantly progressed: applications of full quantum methods are now applicable to polyatomic systems up to 10–20 nuclear degrees of freedom, often combined with *ab initio* method calculations of the electronic structure. For larger systems, semiclassical dynamics such as mean field Ehrenfest dynamics[4] or the widely used trajectory surface-hopping methods, as proposed by Tully,[5] are most often used.

An especially challenging situation is met when many electronic levels (a few tens up to about a hundred) are coupled to a system with many nuclear degrees of freedom. Among the difficulties, numerous competing nonadiabatic channels are opened and the dynamics may proceed within a diversity of time scales. Such processes are likely to occur in the interaction of atomic or molecular systems with surfaces, where the energy deposited on the adsorbate can migrate to various channels (intramolecular and also electronic or vibrational excitation of the substrate) with very different time scales. Clusters in the gas phase offer very convenient systems to investigate such processes, as theoretically exemplified in a recent multiscale dynamical approach of the ionization/fragmentation dynamics of rare gas clusters.[6]

Electronically excited metal atom embedded in a van der Waals cluster of large size may be considered as benchmark systems to address such situations. The electronic degrees of freedom are centered on the atom essentially and the couplings between electronic states are promoted by the interaction with the cluster environment. Many experimental and theoretical works have considered such systems, focusing the attention on the coupling between low lying excited states of the atomic species. Experimentally, this corresponds, for example, to cluster isolated chemical reaction[7] (CICR) experiments. Typically, alkaline earth[8–12] and potassium[13] atoms are deposited at the surface of argon clusters (the case of helium droplets is examined in Refs. 14–21). Theoretical approaches examined the photoinduced dynamics of these systems.[12,22,23] Other theoretical works examined more complex situations where a diatomic molecule is photoexcited on or embedded in argon clusters. In the latter case, a diversity of processes was examined such as dissociation,[24,25] recombination,[24,26,27] and spin nonconserving transitions,[24] and information was given on the factors influencing them such as size and local environment.

The early CICR experiments were carried out on $Ba(Ar)_n$ clusters (*n* ranges between a few hundreds and a few
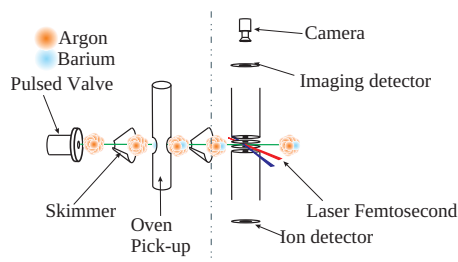
---

a)Electronic mail: jean-michel.mestdagh@cea.fr.

133, 054307-1

FIG. 1. Scheme of the experimental setup.

thousands) and an electronic excitation in the vicinity of the Ba($6s^2$ $^1S \to 6s6p$ ^1P) resonance transition. The initial question of the location of barium concluded to a surface location,[8,9] as for Ca(Ar)$_n$ (Ref. 11) and K(Ar)$_n$.[13] Further experiments showed that the electronic excitation of barium at the surface of the Ar cluster induces dynamics, where two fluorescence channels are observed. Both correspond to the Ba($6s6p$ $^1P \to 6s^2$ ^1S) emission, but in one case the Ba atom is solvated within the cluster, whereas in the other, it is free after ejection out of the cluster.[10] The experimental work was complemented by molecular dynamics simulations of Ba(Ar)$_{125}$ clusters, associated with a surface-hopping method.[12] The dominant process appeared to be a relaxation, in less than 10 ps, toward the lowest of the three nearly degenerate electronic states correlating to the $6s6p$ ^1P excitation of Ba and that the ejection of barium out of the cluster is a rare and delayed event. Unfortunately, the corresponding real-time dynamics has not yet been documented experimentally. Recently, some of us have simulated the photoelectron spectra which would be obtained in a pump pulsed excitation of calcium at the surface of an argon cluster in the vicinity of the $4s4p$ ^1P atomic line, followed by a probe pulsed ionization of the system.[23]

The present work aims at investigating such a benchmark system in the real-time domain. It documents the dynamics of a single barium atom, highly excited in the vicinity of the $6s9p$ state, in the environment of a large argon cluster. We shall see that a variety of behaviors can be disentangled, which proceed at a diversity of time scales ranging over almost two decades, from subpicosecond to a hundred picoseconds. The objective of the present work is simply to highlight the main phenomena involved in the full dynamics. Further experimental works are planned to focus on each phenomenon individually. Similarly, a full theoretical modeling of the dynamics is beyond the scope of the present work. Instead, as a help to discuss the experimental results, *ab initio* calculations of ground and excited states of the Ba$^+$–Ar and Ba–Ar pairs are performed, up to the Ba$^+$($5d$)+Ar and Ba($6s9p$ ^1P)+Ar separation limits, using a pseudopotential approach. An additive pair model is used also to determine the most stable structures for the neutral and cationic BaAr$_n$ clusters in their respective ground state.

II. EXPERIMENTAL

The experimental setup is schemed in Fig. 1. It associates (i) a pulsed molecular beam source generating the argon clusters, (ii) a pick-up source to deposit barium on the clus-

ters, and (iii) an interaction zone with the pump and probe laser beams. It is essentially the same as that used in Refs. 28 and 29. The pick-up source is novel. It is described extensively.

The argon gas is expanded into vacuum using a pulsed valve operating at 20 Hz through a nozzle with a diameter of 100 μm. This generates a beam carrying a log-normal distribution of clusters with an average size of ~750 atoms[7] and a temperature of 32 ± 2 K.[30]

The pick-up source consists of a boron nitride crucible maintained in an oven. The crucible is filled with barium chips, taken from a barium rod (1 cm diameter $\times$ 2 cm long) of 99% quality (Sigma-Aldrich). The operation of cutting the chips and putting them into the crucible is done under a nitrogen enriched atmosphere to prevent reactions with oxygen and water. The oven is heated between 480 and 500 °C. Varying this temperature allows the vapor pressure of barium to be adjusted and, hence, the average number of barium atoms deposited per cluster. Here, significantly less than one Ba atom, on average, is deposited per cluster. Given that the pick-up deposition obeys a Poisson statistics, the number of clusters carrying more than a single Ba atom is negligibly small.

The experiment, of the pump-probe type, is carried out using the LUCA femtosecond laser at the Saclay Laser-Matter Interaction Center Facility. It associates a Ti:sapphire oscillator and amplifiers. It operates at 792 nm [full width at half maximum (FWHM) of 22 nm], with a 20 Hz repetition rate and delivers pulses of ~50 fs duration. A fraction of the output is tripled. Because of the large spectral width of the femtosecond laser and the dispersion of group velocity in the crystals, the frequency multiplication does not act on the central wavelength of the Ti:sapphire oscillator. The tripling here provides pump pulses at 266.3 nm (FWHM of 2.1 nm). The residual output serves to probe the system by single and double photon ionization at 792 nm. Its focusing is adjusted to get a peak power density of ~10^{11} W cm^{-2}. The probe can be doubled also, then the system is probed by a single photon ionization at 399.2 nm (FWHM of 5 nm). The probe laser beam is passed through a delay line to vary the time delay between the probe and the pump pulses (noted delay time hereafter). The cross-correlation between the pump and the probe laser pulses, measured in the interaction region with the cluster beam, is ~80 fs.

The pump and probe laser beams overlap each other as they cross the cluster beam. This region is also the ionization region of both a time of flight ion mass spectrometer and a velocity map imaging (VMI) system. The latter is used only in the present experiment. It maps the kinetic energy and the angular distributions of the charged particles resulting from the ionization by the probe laser.[31] It is adapted to detect either the photoelectron or the photoions, depending on the sign of the extraction and acceleration voltages. Photoelectrons and photoions are detected on a position sensitive detector, creating raw images that are recorded for each pump-probe delay and accumulated over several hundred laser shots. Each raw image is a two-dimensional (2D) projection of the actual three-dimensional (3D) distribution. Thanks to the cylindrical symmetry about the direction of polarization
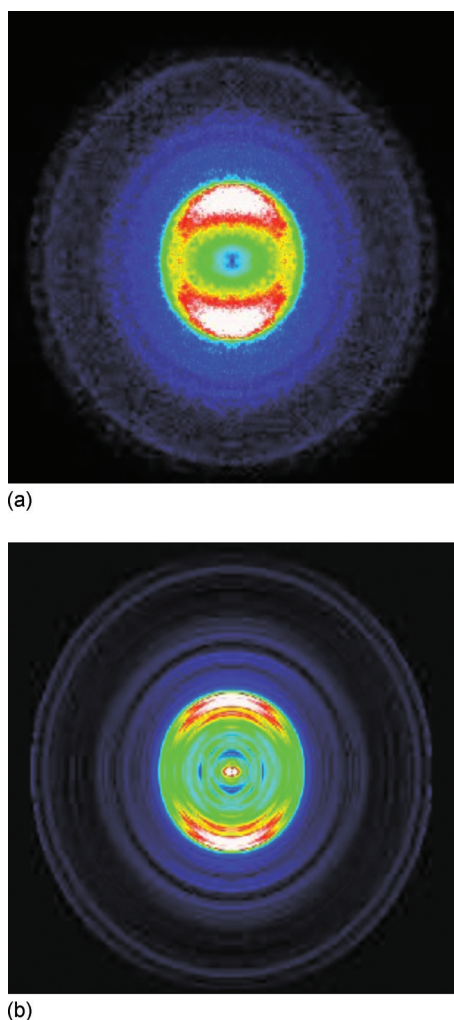
(a)

(b)

FIG. 2. Raw (a) and pBASEX inverted (b) electron images with the delay time of $t=70$ ps. The radial distance in the inverted image is proportional to the velocity of the photoelectrons and the angle corresponds to their direction of emission with respect to the polarization of the probe laser (vertical) in the figure.

of the probe laser, which is parallel to the cluster beam, the pBASEX algorithm is used to reconstruct the 3D distribution from the 2D image.[32] This provides the inverted image, which contains the pertinent information of the 3D distribution, i.e., the velocity and the angular distributions of the charge particles (electrons or ions), which are detected.

Typical raw and inverted images of photoelectrons are shown in Fig. 2. The radial distribution represents the velocity distribution of the electrons, whereas the angular distribution reflects the anisotropy of the electron distribution. The anisotropy is not considered in the present work. It will be studied in a forthcoming work, which will focus on the orientation and alignment effects in the excited barium dynamics. Hence, when considering the inverted images in terms of a development in Legendre polynomial with respect to the electron scattering angle, only the zeroth order is considered. This provides a photoelectron velocity distribution, which is easily converted into an energy spectrum: the photoelectron spectrum. The photoelectron spectrum, which has been extracted from Fig. 2, is shown in Fig. 3. A full experiment consists of recording such spectra as a function of the pump-probe delay.
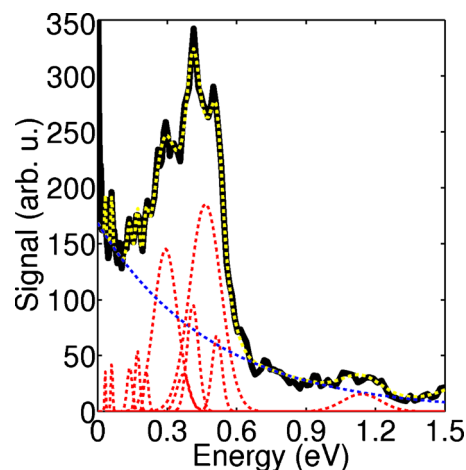

FIG. 3. Experimental photoelectron spectrum at $t=70$ ps (black solid curve) and its processing by the decomposition method (dashed curves): unstructured continuum signal (blue), Gaussian peaks (red), and reconstructed spectrum (yellow).

Photoions are selected at the $^{137}Ba^+$ mass by pulsing the detector. As for the photoelectrons, the radial and angular distributions in the inverted images document the velocity and angular distributions of the ions.

III. EXPERIMENTAL RESULTS

A. Photoelectron spectra

A series of photoelectron spectra was recorded as a function of the delay time. A small signal was observed between 0.1 and 0.3 eV electron energy when only one laser is present, either the pump or the probe. It is due to multiphoton ionization by these lasers. It acts as a baseline to the time dependent signals observed in the pump-probe experiment. It has been subtracted from the photoelectron spectra shown as a 3D plot with false colors in Fig. 4: the color reflects the signal intensity as a function of the photoelectron energy (vertical axis) and delay time (horizontal axis). Various energy bands are observed in the figure, whose intensity varies
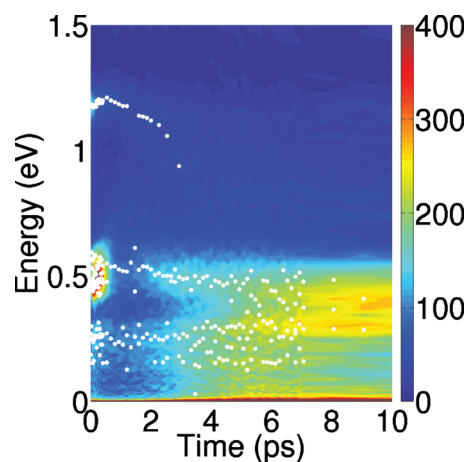

FIG. 4. 3D plot of the photoelectron data: the electron signal (shown as false colors with the scale shown on the right side of the figure) is plotted as a function of the electron energy (vertical axis) and delay time (horizontal axis). The white points are the center of the Gaussian peaks found after processing the data using the decomposition method.
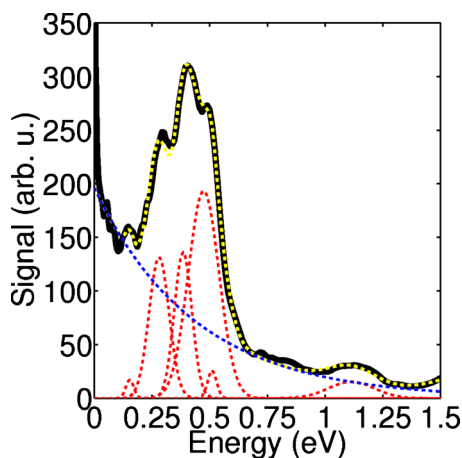
FIG. 5. Averaged photoelectron spectrum corresponding to the measurements performed at delay times $t > 7$ ps (black solid curve). Otherwise, the same caption as in Fig. 3.

FIG. 6. Ba^+ ion signal as a function of the delay time t (black solid curve). The blue dashed curve shows the probability density function f of the detection (see Sec. VI C for details).

with the delay time. An intense band close to ~0.5 eV is observed over the first 0.5 ps, whereas a series of bands, with energies ranging between 0 and 0.6 eV, grows slowly over the time range of 0–3 ps. They grow more rapidly after 3 ps and reach an almost constant intensity after 7 ps. Strikingly, a band seems to be shifting in energy from 1.2 eV at a delay time $t = 0$ ps down to 1.0 eV at 4 ps. The latter observation will be substantiated by a refined data analysis in Sec. IV C. Since the electron spectrum is stationary beyond 7 ps, the signals recorded at delay times $t > 7$ ps were averaged and the resulting spectrum is shown in Fig. 5. It reveals a complex band system.

A time dependent signal associated with photoelectrons of ~0.6 eV energy is observed at negative delay times. It corresponds to a reverse function of the pump and probe, the light pulse at 792 nm acting as the pump, probably in a multiphotonic excitation process, and that at 260 nm acting as the probe. This corresponds to a different photophysical process than that explored in the present paper. It is not considered here.

A similar study was performed with the probe laser at 399.2 nm (3.11 eV) (not reported in the figure). The band systems with energies ranging between 0 and 0.6 eV observed in Fig. 4 with the 792 nm probe are observed again with the 399.2 nm probe and have the same dependence on the delay time.

B. Photoion signal

Considering the large mass of the $Ba(Ar)_{\approx 750}$ clusters, more than $\approx 32\,000$ amu, unfragmented ionized clusters cannot be deflected into the VMI, which is perpendicular to the beam. Only much smaller cluster ions or Ba^+ ions reach the detector and lead to an ion signal.

The multiphotonic one-color ionization of the cluster beam by the pump laser produced Ba^+ ions and $Ba^+Ar_{\leqslant 10}$ cluster ions, which were observed using the procedure described in Ref. 29. In contrast, only Ba^+ ions were observed in the pump/probe experiment when the delay time is set to more than 5 ps. Hence, whatever the delay time, only the Ba^+ ions are considered hereafter. Importantly, the corresponding
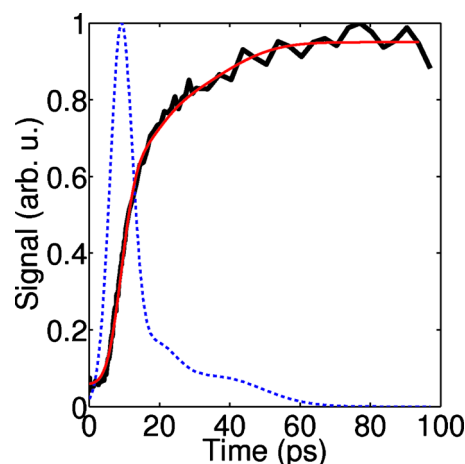
ion count was significantly smaller than the electron count at the same delay time. This suggests that most of the ions produced by the ionization do not correspond to Ba^+ but to heavy cluster ions, which do not reach the detector.

As will appear in the discussion, the Ba^+ ions mentioned in the previous paragraph are produced by the ionization of excited barium atoms, which have been ejected out of the clusters after excitation by the pump laser. A series of Ba^+ photoion images was recorded as a function of the pump-probe delay time t. The full ion signal, obtained by integrating each image over the ion scattering angle and velocity distribution, is shown in Fig. 6 (black solid curve). The individual ion images reveal an isotropic angular distribution of the photoions and a velocity distribution, which changes very little with t. For the purpose of the present work, it is sufficient to consider the velocity distribution obtained after averaging all the images. It is shown in Fig. 7 and reflects essentially the velocity distribution at delay times larger than 5 ps, where the ion signal is large. It is adequately fitted by a Maxwellian velocity distribution at a temperature of 495 ± 6 K, indicating that the ejected barium atoms have a thermal energy of 0.064 eV.
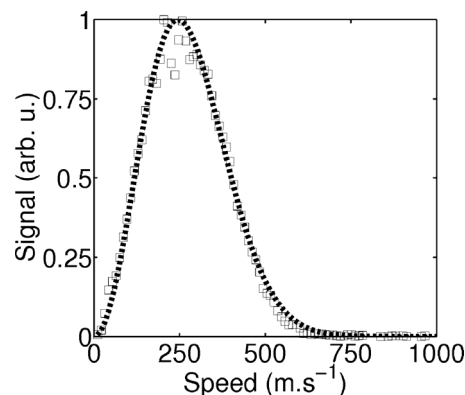

FIG. 7. Velocity distribution of the Ba^+ ions (open squares). Best fit by a Maxwellian velocity distribution (dashed curve) corresponding to a temperature of 495 K.

IV. ANALYSIS OF THE PHOTOELECTRON DATA

The photoelectron data consist of a series of electron spectra taken at various delay times. Such a spectrum is shown in Fig. 3. It consists of a series of peaks superimposed on a broad unstructured continuum. The latter is maximum at 0 eV and seems to decrease exponentially as a function of energy. An issue in the present work is to check whether the energy of the peaks, which is associated with specific energy states of barium in the argon environment, varies as a function of the delay time. For this reason, a statistical method combining a Bayesian modeling of the problem and a Monte Carlo Markov chain (MCMC) optimization algorithm has been used to analyze each spectrum and to extract meaningful information on both the continuum and the peaks. This method, called decomposition method below, has already been applied successfully to disentangle complex infrared and Raman spectra.[33] Note that the number of peaks and the position and width of each peak are *a priori* unknown. A brief outline of the decomposition method is given here. A full description will appear elsewhere.

A. Decomposition method

The problem of estimating the peaks in a single spectrum is considered as an object extraction problem: each spectrum is modeled as a sum of an unknown number of peaks, each peak having its own amplitude, location, and width, superimposed on an unstructured exponentially decreasing continuum. Hence, the experimental data $y(e)$ are fitted by

$$y(e) = \sum_{k=1}^{K} a_k f_{c_k, w_k}(e) + \alpha \exp\left(-\frac{e}{\beta}\right) + n(e),\qquad(1)$$

where e denotes the electron energy; c_k, a_k, and w_k correspond to the positions, amplitudes, and widths of peak k, respectively; α and β describe the exponentially deceasing continuum; $n(e)$ models the experimental noise and the model imperfections; and finally, the function f represents the shape of the peaks, which is assumed to be Gaussian.

From a theoretical point of view, the problem is ill-defined in the sense of Hadamard because of the nonlinearity of the model and the unknown number of variables. It is set within the Bayesian framework.[34,35] Accordingly, $\theta = \{a_{k=1,\ldots,K},\ c_{k=1,\ldots,K},\ w_{k=1,\ldots,K}, \alpha, \beta, n\}$ and the data y are assumed to behave as randomly distributed variables. The Bayes theorem relates the *likelihood* $P(y|\theta)$, the *prior* $P(\theta)$, and the *posterior* $P(\theta|y)$ according to

$$P(\theta|y) = P(y|\theta) \times P(\theta)/P(y).$$

The key idea of the data analysis is to include all the information, which is available on θ and y. Note that y represents the experimental results. It is therefore not a random variable and $P(y)=1$. The priors $P(\theta)$ are distribution functions chosen *a priori* for each parameter (see Sec. IV B). The likelihood $P(y|\theta)$ is the deviation from a typical distribution of the noise $n(e)$, calculated from the difference between the signal and the fit functions. The noise $n(e)$ is expected to be white, zero-mean Gaussian, independent and identically distributed with variance r_n.

This model is well-adapted to the present problem but it leads to a difficult optimization task because of the existence of a number of local minima due both to the high-dimensionality and the nonconvex behavior of the posterior. This has motivated the use of a MCMC simulation technique to achieve the estimation. Since the number of peaks is an unknown, MCMC has to deal with model uncertainty. The reversible jump MCMC algorithm[36,37] appears to be the most flexible and popular method for this purpose. This algorithm has the ability to "jump" between spaces of different sizes, thanks to moves proposed by the user. At each iteration of the MCMC algorithm, one of the three following popular moves is equiprobably chosen as in Ref. 36: (i) creating a new peak with parameters randomly drawn, (ii) removing a randomly chosen peak, and (iii) updating the parameters of an existing peak.

In cases (i) and (ii), a jump is accepted according to a restriction rule based on the assumption that the normalized number of peaks in a spectrum K/K_{max} is distributed according to a beta distribution $\mathcal{B}e(1, K_{max}+1)$ (where K_{max} is the maximum number of peaks in a spectrum). This prevents one to sample situations with an unrealistically large or small number of peaks to fit the experimental spectrum. In case (iii), a Gibbs sampler is implemented.[38] It consists of simulating each variable according to its conditional posterior distribution. The MCMC algorithm was run for 2×10^4 iterations, in less than 1 min with MATLAB on a dual core 2×3.8 GHz PC. At each iteration, the new set of parameters is stored, together with the corresponding likelihood $P(\theta|y)$. The solution is chosen among the bench of parameter sets using the following procedure. A histogram is built, giving the number N_p of sets, which contains p peaks. The best fit solution is taken from the sets associated with the largest N_p number in the histogram. Among them, the best solution is chosen as that of highest posterior $P(\theta|y)$.

B. Bayes prior distributions

As said above, the prior distributions were chosen to include the available information about the variables. Moreover, the distribution functions used for the priors were chosen to allow for convenient calculations of the corresponding conditional posteriors.[38] The priors are listed hereafter.

(i)   No information is *a priori* available about the peak locations c_k, so the peaks are assumed to be uniformly distributed over the energy set.

(ii)   Peak amplitudes a_k are necessarily positive, so they are distributed according to a normal distribution (which is conjugate for the amplitudes) with mean 0 and variance r_a, truncated to get positive amplitudes.

(iii)   Peak widths w_k are also positive. They are distributed according to an inverse gamma prior $\mathcal{IG}(\alpha_w, \beta_w)$, whose parameters can be set using a preprocessing method or according to physical knowledge.

(iv)   The parameters α and β describing the exponentially decreasing continuum are assumed to be distributed

according to a gamma distribution $\mathcal{G}a(\varepsilon,\varepsilon)$ with ε =0.01≪1 so as to favor large values.

(v) The hyperparameter r_a is distributed according to an inverse gamma prior $\mathcal{IG}(\alpha_a=0.01,\beta_a=0.01)$, whose mean is set to a rough estimation of the amplitude and the variance is large.

(vi) Finally, we adopt an inverse gamma prior $\mathcal{IG}(\alpha_n,\beta_n)$ for the noise variance r_n, whose parameters are both set close to zero (usual choice for noise variance).

C. Results of the data analysis

The decomposition method was applied to each of the photoelectron spectra, which were recorded as a function of the delay times t. The efficiency of the method is illustrated in Fig. 3 for the spectrum taken at $t=70$ ps. The dashed yellow curve shows the reconstructed spectrum. As explained in Sec. IV B, the analysis takes the experimental resolution into account, which is given by $\pm 0.075 \times E_e$, where E_e is the electron energy in eV. The noise filtering by the decomposition method is therefore more efficient at high energy since the expected photoelectron bands are much broader there than the peaks due to the experimental noise. Accordingly, the yellow curve washes out most of the experimental noise above 0.6 eV. In contrast, several estimated peaks at lower energies do not correspond to the actual photoelectron bands. This is apparent when comparing the data analysis of a series of spectra taken at adjacent delay times. Peaks, which are associated with the experimental noise, are indeed not reproducible from one spectrum to the other.

The locations of the peaks found by the decomposition method [c_k in Eq. (1)] are indicated by white points in Fig. 4. Due to the experimental noise discussed above, these points are scattered within the colored bands corresponding to the most intense photoelectron signal. The important point here is that the decomposition method confirms quantitatively the qualitative observations done in Sec. III A. In particular, the behavior of the photoelectron band, which shifts in energy, can be refined. Its energy increases slightly from 1.18 to 1.21 eV between time $t=0$ and $t=0.5$ ps, then decreases, and reaches 0.93 eV at $t=2.9$ ps. After 2.9 ps, this band "dissolves" into the background and cannot be documented further.

Figure 5 shows the average photoelectron spectrum at delay times $t>7$ ps (black solid curve) and its processing by the decomposition method. The signal/noise ratio is much larger in the average spectrum compared to individual spectra and the experimental noise is filtered fully by the data analysis. Five electron bands are found, peaking at 0.15, 0.28, 0.38, 0.47, 0.51, and 1.1 eV.

Data, which are not presented here, taken with a 399.2 nm probe, were also analyzed using the decomposition method. The electron bands found at delay times $t>7$ ps are centered at the same energies, 0.15, 0.28, 0.38, and 0.50 eV, as above with the 792 nm probe. This confirms the anticipation at the end of Sec. III A that a two-photon probe is performed at 792 nm when $t>7$ ps. The exponentially decreasing continuum is also present in the 399.2 nm probe experiments with the same time behavior as in the 792 nm probe experiments. Again, this is the indication that the 792 nm probe acts through a two-photon ionization process to generate this signal.

V. Ba–Ar AND Ba⁺–Ar POTENTIAL ENERGY CURVES

The purpose here is to provide elements concerning Ba–Ar and Ba⁺–Ar potential energy curves, which will be useful for the discussion of the experimental data shown in the sections above. The pump laser at 266.3 nm provides the Ba(Ar)$_{\approx750}$ system with 4.66 eV electronic energy, which is likely localized on barium. Hence, Ba–Ar potential energy curves up to this energy will be considered in the discussion. A work by Czuchaj *et al.*[39] documents the Ba–Ar system, but only low lying molecular states up to the Ba($6s6p\ ^1P$)+Ar dissociation limit (2.24 eV). Here, a calculation of the Ba–Ar molecular states, up to those correlating with Ba($6s9p\ ^1P$) +Ar, was performed, together with that of the six lowest molecular states of Ba⁺($6s,5d$)+Ar. The calculations were performed at Ba–Ar distances ranging between 0.2 and 5.3 nm. Only results, which are relevant for the discussion of the Ba(Ar)$_{\approx750}$ dynamics are presented below. A full account of the Ba–Ar and Ba⁺–Ar potential energy calculations will appear in a forthcoming paper.[40]

A. Calculation method

The calculations were performed using the CIPSI package.[41,42] The method used to calculate the Ba–Ar potential energy curves is similar to that used in our previous work on the Ca–Ar system[43] and also in investigations of other authors[39] dealing with excited states of BaAr up to $6s6p\ ^1P$. The electronic problem is reduced to two valence electrons moving in the electric field created by two polarizable cores, Ba²⁺ and Ar. An effective core potential (ECP) describes the interaction of a single electron with Ba²⁺. It is complemented by core polarization potentials (CPPs) to account for the polarizability of the two cores. The ECP, the adapted basis set, and the CPPs will be presented in Ref. 40. Note that the basis set includes an extensive set of diffuse functions to ensure a satisfactory description of the Rydberg orbitals. The correlation of the two electrons was treated at the full-CI level. The total energy of the system was obtained by adding the Ba²⁺–Ar core-core interaction energy to the energies provided by the valence full-CI calculation. The latter was obtained in a separate pseudopotential calculation with eight active electrons on Ar at the CCSD(T) level for electronic correlation. The latter calculation will also be presented in a forthcoming paper.[40]

The potential curves of the one active-electron Ba⁺($6s,5d$)+Ar were calculated using the same basis, pseudopotentials, and CPP. The reliability of the calculation in providing a realistic representation of the high energy levels of barium was evaluated in regard to the available spectroscopic data on the Ba atom. A full account of the comparison will be given in Ref. 40. Briefly, 80% of the calculated energies agree with the experimental values within ± 200 cm⁻¹. Table I lists the comparison results for some Ba and Ba⁺ states, which are relevant for the interpretation of the present experimental results.

TABLE I. Term symbols of Ba and Ba$^+$, which are relevant to the present work. The column labeled Δ is the energy difference between experiment (Expt.) and calculation (Calc.). All energy values are given in cm^{-1}. They are taken from the ground state Ba.

State	Calc.[a]	Expt.[b]	Δ
		Ba	
$6s7s\ ^1S$	28 130	28 230	-100
$5d6p\ ^1P$	28 640	28 554	86
$6s9p\ ^1P$	37 615	37 775	-160
		Ba$^+$	
$6s\ ^2S$	41 920	42 035	-115
$5d\ ^2D$	47 405	47 389	16

[a]This work, full-CI calculations.
[b]References 44 and 45.

B. Molecular states

A few potential energy curves are shown in Fig. 8. They reflect the main categories of curves encountered in the full calculation. For the lowest states, the present results are in agreement with the previous calculation of Czuchaj *et al.*[39] The ground state potential appears in Fig. 8 (bottom panel). It is has a shallow well of 95 cm^{-1} depth at a fairly large Ba–Ar distance of 0.55 nm. Except at very short distances, it is well separated from the upper states. The middle panel of Fig. 8 displays potential curves, which dissociate into barium states with about 3.5 eV excitation energy. One of theses states is singly excited ($6s7s\ ^1S$) and the other is doubly excited ($5d6p\ ^1P$). Importantly, the $^1\Sigma^+$ states in this energy region are fairly repulsive at Ba–Ar distances smaller than 0.4 nm. This generates anticrossings with upper $^1\Sigma$ curves.
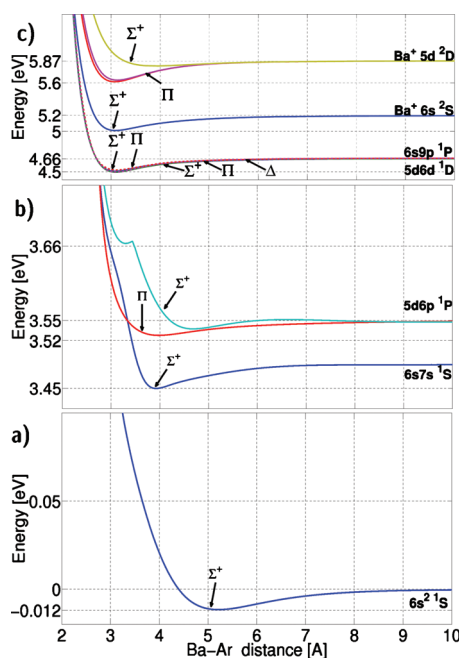

FIG. 8. Calculated potential energy curves of Ba–Ar and Ba$^+$–Ar. Only a representative sample of the potentials relevant for the present work is shown in the figure. The three panels correspond to three energy ranges, the bottom one corresponding to the ground state curve. Eight curves are correlated with the $5d6d\ ^1D$ and $6s9p\ ^1P$ states in the top panel. They show up as a single curve at the scale of the figure.

The apparent cusp along the $^1\Sigma^+$ curve correlating with $5d6p\ ^1P$ in the middle panel of the figure is due to such an anticrossing with a higher state, not shown. States correlating with barium states in the 3.6–3.9 eV range experience many anticrossings, hence generating a region where many states, not only those of $^1\Sigma^+$ symmetry, are coupled together. The top panel of Fig. 8 displays the situation encountered at larger energies where molecular states are correlated with either Rydberg states Ba($6s9p\ ^1P$) (Rydberg) or doubly excited states of barium and Ba($5d6d\ ^1D$) (double excitations). They show up as almost superimposed at the scale of the figure and run almost parallel to the ground state curve of the Ba$^+$–Ar molecular ion, which also appears in the figure.

The present calculation of potential energy curves of BaAr diatomics is not meant to mimic directly the energy states of the BaAr$_{\approx750}$ clusters. More simply, it intends to provide useful hints for the discussion. Moreover, it will be used to design pair potential models in clusters (see below for ground state neutral and cationic cluster optimization).

VI. DISCUSSION

The experimental results reported in Sec. III document both the photoelectron spectrum of the Ba(Ar)$_{\approx750}$ system as a function of the delay time and the appearance of an ion signal corresponding to Ba$^+$ at delay times larger than 5 ps. The energy distribution of these ions was also measured. The discussion of these results is organized as follows. First we discuss the initial electronic state of the Ba(Ar)$_{\approx750}$ system, which is created by the pump laser (Sec. VI A). Using the observation of the Ba$^+$ ions and the calculation of the Ba–Ar potential energy curves as guidelines, we discuss qualitatively the early dynamics of barium, after excitation by the pump laser (Sec. VI B). Then we discuss the ejection of barium as a consequence of nonadiabatic energy transfers (Sec. VI C). For a full dynamical information on the relaxation process, which pushes barium out of the cluster, Sec. VI D examines the partitioning of the available energy between electronic energy and kinetic energy of the ejected barium. Finally, Sec. VI E examines the variation of the electronic energy during the early dynamics discussed in Sec. VI B.

A. Initial state of the Ba(Ar)$_{\approx750}$ system

A former work showed that a single barium atom trapped on an argon cluster of about 2000 atoms is located at the surface of the cluster.[8,9] Given the similarity between the present experiment and that in Ref. 8, we consider that here too, Ba is located at the cluster surface.

The excitation energy provided by the pump laser at 266.3 nm to the Ba(Ar)$_{\approx750}$ cluster is 4.66 eV (37 552 cm^{-1}). The state of free barium, which is closest to this energy and accessible from the ground state through an allowed electric dipole transition, is $6s9p\ ^1P$, a Rydberg state with a 37 775.28 cm^{-1} excitation energy.[46] As discussed now, the cluster environment is expected to split the $6s9p\ ^1P$ state, to shift the resulting states down in energy, and to mix them with nearby states, thus achieving close resonance with the pump laser.

TABLE II. Potential energy (in eV) of $Ba(6s^2\ ^1S)-Ar_{55}$ and $Ba^+(6s\ ^2S)-Ar_{55}$ under the geometries G_1 and G_2. The zero of energy corresponds to Ba (or Ba^+ at infinite separation from the Ar_{55} cluster). G_1 corresponds to the optimized geometry of $Ba(6s^2\ ^1S)-Ar_{55}$ and G_2 to that of $Ba^+(6s\ ^2S)-Ar_{55}$.

	$Ba(6s^2\ ^1S)-Ar_{55}$	$Ba^+(6s\ ^2S)-Ar_{55}$
G_1	−0.17	−0.27
G_2	+2.28	−1.14

Two limiting situations of a Rydberg state solvated by a rare gas environment is evoked now to help the discussion. The first one is matrix isolation and the second is solvation by a small finite cluster. A contrasted situation is met in matrices according to the principal quantum number n of the Rydberg state.[47–50] At low n values, the Rydberg orbital do not have enough space to develop because the matrix acts as a cage. Repulsive interactions are dominant and the Rydberg states are shifted to higher energies. In contrast, for large n values, the Rydberg orbital encompasses atoms of the matrix and somehow "dilutes" inside the matrix, and a cutoff of the number of Rydberg states is observed.[47–50] The situation, which is encountered in small clusters, is much simpler. It was studied by Ben El Hadj Rhouma *et al.* in a pseudopotential quantum-classical approach.[51] Here, Na is excited in the $4s$ and $5s$ Rydberg states and interacts with small argon clusters ($NaAr_n^*$ with $n \le 10$). Since the size of the clusters is much smaller than that of the Rydberg orbital, the latter is free to develop about the cluster and the highly excited $NaAr_n^*$ cluster consists of a central Na^+ ion, solvated by an argon shell, surrounded by the diffuse Rydberg electron. As a result, a substantial stabilization of the Rydberg states is predicted since the Na^+-cluster polarization forces add to the Na^+-electron Coulomb attraction.

Turning back to $BaAr_n$ clusters, geometry optimizations of the ground electronic state of the $Ba(6s^2\ ^1S)Ar_{55}$ and $Ba^+(6s\ ^2S)Ar_{55}$ clusters were performed. A Monte Carlo type optimization method[52] was used involving pair-additive potential energy functions, namely, the calculated Ba–Ar (or Ba^+–Ar) potentials obtained above and the potentials in Ref. 53 for the Ar–Ar pair. The most stable geometry for the ground state neutral cluster shows barium located at the cluster surface, whereas in the cationic cluster, Ba^+ is located in the interior. Table II shows the energies of $Ba(6s^2)Ar_{55}$ and $Ba^+(6s\ ^2S)Ar_{55}$ calculated at two different geometries, G_1 and G_2, corresponding to the optimized geometry of $Ba(6s^2)Ar_{55}$ and $Ba^+(6s)Ar_{55}$, respectively. Thus, in a rather small cluster such as $BaAr_{55}$, and for a diffuse orbital larger than the cluster size, one expects the occurrence of Rydberg states with stable geometries close to those of the cation, in line with the above consideration on small $NaAr_n^*$ clusters.

In the larger clusters, which are considered in the present experiment, $Ba(Ar)_{\approx 750}$, given the surface location of barium, the $9p$ Rydberg orbital of the $Ba(6s9p\ ^1P)$ state, which is believed to be populated by the pump laser, is neither caged nor totally free to develop. This orbital has indeed a half empty space to develop and the other half space is partly occupied by the finite size cluster. The radius of the $9p$ orbital is expected to be close to the size of the cluster,

≈ 1.7 nm versus ≈ 2 nm (these orders of magnitude were obtained, assuming a quantum defect of 3.48 for the $9p$ orbital of barium[54] and a cfc structure to the argon cluster with a lattice parameters of 0.534 nm). The partly occupied half space is expected to play two roles. The first one is to stabilize the $Ba(6s9p\ ^1P)$ Rydberg state. The two redshifting effects mentioned above may be at play, i.e., the large n Rydberg effect in matrices and the effect encountered with small $NaAr_n^*$ clusters. In both cases, most of the stabilization of the $Ba(6s9p\ ^1P)$ Rydberg state would be due to the Ba^+ core underneath the $9p$ orbital, which polarizes the argon atoms of the cluster. The second role of the partly occupied half space, because the environment of barium is nonspherical, is to distort the $9p$ orbital, hence making the pump laser populate a superposition of $6s, nl\lambda$ states in the vicinity of the $6s9p\ ^1P$ state (with λ being the projection of the electronic orbital angular momentum along the "barium-cluster coordinate"). The $6s5f\ ^1F$ and $5d6d\ ^1D$ states, which are located at -36 and 62 cm^{-1} from $6s9p\ ^1P$, respectively, are likely candidates for such a state mixing and the initial state is likely a superposition of the $6s9p$, $6s5f$, and $5d6d$ configurations, shifted down in energy by the interaction with the cluster. Given the degeneracy of the $6s9p\ ^1P$, $6s5f\ ^1F$, and $5d6d\ ^1D$ states, it is conceivable that their mixing by the cluster environment forms a series of nearly degenerated states, which are accessible from the ground state by an electric dipole transition. Given the spectral width of the pump laser (2.1 nm), the initial wavepacket is likely a coherent superposition of several multiconfigurational electronic eigenstates of the barium-cluster system, built from the mixing of the $6s9p\ ^1P$, $6s5f\ ^1F$, and $5d6d\ ^1D$ states of free barium and redshifted with respect to $6s9p\ ^1P \leftarrow 6s^2\ ^1S$ transition by the interaction with the cluster.

A photoelectron signal, with bands at 1.18, 0.59, and 0.46 eV, is observed in Fig. 4 during the cross-correlation time between the pump and the probe laser pulses. It corresponds to a resonant 266.3 nm+792 nm ionization of the $Ba(Ar)_{\approx 750}$ cluster, the intermediate resonant state being $6s9p\ ^1P$. The ionization of free $Ba(6s9p\ ^1P)$ by a single 792 nm photon leads to photoelectrons of 1.02, 0.42, and 0.32 eV energy, whether the Ba^+ ions is formed in the $6s\ ^2S_{1/2}$, $5d\ ^2D_{3/2}$, or $5d\ ^2D_{5/2}$ electronic states, respectively. The fact that the latter energies are 0.16 eV smaller than the energy bands in the experimental photoelectron spectrum is consistent with the anticipation above that the Rydberg state $6s9p\ ^1P$ is not shifted significantly by the argon environment, combined with the energetics in Table II, which suggest a lowering of the ionization energy of Ba by 0.10 eV ($0.27-0.17=0.10$), when it is solvated at the surface of the cluster (geometry G_1). According to the ionic core conserving picture, the band at 1.18 eV should be the most intense one if the resonant intermediate state $Ba(6s9p\ ^1P)$ was of pure $6s9p$ configuration. This is not the case experimentally, a consistent observation with the expectation above that the $6s9p$, $6s5f$, and $5d6d$ configurations are mixed.

B. Early time dynamics: Partial embedding of barium into argon

The conspicuous feature of the Ba$^+$ ion signal shown in Fig. 6 is its rapid rise at delay times $t > 5$ ps, whereas it is very small at $t = 0$ and increases only slightly between 0 and 5 ps. This question is discussed in the present section and the next one.

We first consider the diatomic potential energy curves shown in the top panel of Fig. 8. It appears that the interaction of Ba($6s9p$ ^1P) [or Ba($5d6d$ ^1D)] with argon is attractive at Ba–Ar distances larger than 0.3 nm, whatever the alignment of the excited orbital with respect to the Ba–Ar axis. The Σ and Π curves correlating with Ba($6s9p$ ^1P) +Ar, as the Σ, Π, and Δ curves correlating with Ba($5d6d$ ^1D) are indeed almost parallel and all of them are attractive when Ba–Ar > 0.3 nm. This is an effect of the large radius of the Rydberg orbital, which makes the Rydberg electron not "feel" the alignment of Ba–Ar.

We now turn back to barium in the cluster environment. At equilibrium, prior to the laser excitation, the distance between barium atom, which sit at the cluster surface, and the closest argon atoms forming this surface should be close to the equilibrium distance of the ground state Ba–Ar diatomics, 0.55 nm. This geometrical arrangement is not changed by the pump laser excitation, which is vertical. However, after the excitation, barium within the argon environment will start moving on a multidimensional Ba-cluster potential energy surface. The latter is attractive along the Ba–Ar coordinates as discussed above. Hence, the argon environment is getting closer to barium, which will have a tendency to embed into argon.

At this stage, barium does not have a large velocity within the cluster. Upon ionization of the cluster by the probe laser, the Ba$^+$ ion keeps this small velocity with respect to the cluster and is likely to stay solvated, the excess solvation energy being released by the evaporation of a few neutral argon atoms. Hence, at these delays, the probe forms Ba$^+$(Ar)$_{\leq 750}$ cluster ions essentially, which are too heavy to be deflected into the detector. Of course, the corresponding electrons lead a measurable signal. It is examined and discussed in Sec. VI E.

C. Nonadiabatic energy transfers and ejection of barium

Figure 6 and the discussion of the previous section suggest that the dynamical regime where barium is burying inside the cluster lasts about 5 ps, as long as the Ba$^+$ ion signal stays very small. Such a long time scale is not surprising since the considered cluster is rather large. The rearrangement of the argon atoms and the multiple collisions may prevent barium from reaching rapidly optimal locations inside the cluster. After ≈ 5 ps, the Ba$^+$ ion signal increases rapidly, indicating that this regime is competed by a new one where barium is moving out of the cluster. The questions, which are addressed in the present section, are why the dynamics have changed and which mechanism has given an outward velocity to barium?

The previous section has shown that after the excitation by the pump laser, barium is driven inward the cluster along attractive (parallel) potentials. Accordingly, the distance between barium and each of its neighbors switches from ~0.55 nm (the equilibrium distance of the Ba–Ar diatomics in the ground state) to ~0.3 nm (the typical equilibrium distance of the Ba–Ar diatomic Rydberg states). From Fig. 8 (top panel), this movement corresponds to an ~0.15 eV stabilization of the excited barium by each of its neighbors. Due to solvation of the initial excited state by the rearrangement of the argon solvent, the global stabilization energy of excited barium may thus be estimated between ~0.75 eV (surface solvation by 5 argon atoms) and up to 1.8 eV (volume solvation by 12 argon atoms). This lowers the electronic energy from the 4.66 eV, provided by the pump laser, down to ~3.9–2.9 eV, from rough estimations. Alternatively, the states of barium, which are located in the 3.5 eV energy region, do not have a Rydberg character and do not lead to a network of attractive potential energy curves when argon is approached. Instead, the middle panel of Fig. 8 shows, for instance, that the curve correlating with Ba($6s7s$ ^1S) is repulsive and higher by ~0.2 eV when Ba–Ar distances are shortened from 0.55 down to 0.3 nm. Following again an additive estimation, the total energy upward shift for the repulsive states can be estimated between 1.0 and 2.4 eV for 5 and 12 argon neighbors, respectively, moving this state as high as ~4.5–5.9 eV. Hence, a network of surface crossings with dissociative states is expected to be met during the barium-embedding process. The nonadiabatic couplings between the initial attractive states and the repulsive predissociative states are likely to explain the ejection of barium at delay times $t > 5$ ps, which is thus indirect. In this scenario, the electronic energy may be afterward, at least partially, converted into kinetic energy along a dissociative coordinate.

The time dependence of the ion signal shown in Fig. 6 suggests that the ejection of barium and its detection by ionization are complex phenomena. Indeed, if the nonadiabatic energy transfer was active at a well defined geometry of the Ba-cluster system and a well defined time after the excitation by the pump laser, giving a well defined kinetic energy distribution to barium, the Ba$^+$ signal should appear as an erflike function. Actually, Fig. 6 shows that it is not fully the case since the ion signal keeps increasing steadily above 30 ps. This appears more clearly in the probability density function f of the detection, the ion signal S at delay time t being given as the integral $\int_0^t f(x)dx$. The function $f(t)$ is shown as a dashed curve in Fig. 6, indicating that the events, which are detected, fall into two categories, a bell shaped distribution of events peaking at 9.4 ps with a ± 8 ps width and an extremely broad distribution of events extending up to 60 ps. This bimodal shape suggests that the nonadiabatic energy transfers, which finally switch the system onto a dissociative state, do not appear at the same time and are initiated by a complex dynamics (multicrossing situations).

D. Electronic and kinetic energy distribution of barium after the ejection

From the previous section, it appears that 5 ps after the excitation by the pump laser, barium starts to be ejected out

of the cluster. The ejection events are essentially achieved within 7 ps and a large fraction of the barium atoms does no longer interact with argon, with the result that their electronic energy distribution remains constant. This picture is consistent with the observation in Fig. 4 that the photoelectron spectra do not evolve at delay times $t > 7$ ps.

Applying the decomposition method to the average spectrum of Fig. 5 at delay times $t > 7$ ps reveals five electron bands at 0.15, 0.27, 0.38, 0.47, 0.51, and 1.11 eV superimposed onto an exponentially decreasing continuum. We first examine the possibility that these bands are due exclusively to free barium atoms, after ejection out of the cluster. We have discussed in Sec. IV C that a two-photon ionization process at 792 nm is responsible for these bands, thus providing 25 326 cm^{-1} (3.14 eV) for the ionization, in addition to the barium electronic energy. A series of singlet and triplet states of barium corresponding to the $6s6p$, $6s7s$, $5d6p$, and $5d^2$ configurations, ranging between $6s6p\ ^1P$ at 18 060 cm^{-1} to $5d6p\ ^1F$ at 26 816 cm^{-1}, might account for the five electron bands observed experimentally. To be quantitative, a simulation of the photoelectron spectrum has been performed, assuming the following: barium atoms with $6s6p$ and $6s7s$ configurations are ionized to Ba$^+(6s\ ^2S)$; those with $5d6p$ configuration are ionized to Ba$^+(5d\ ^2D_{3/2,5/2})$; the ionization efficiency of a barium state is proportional to its degeneracy; the electron signal corresponding to the ionization of these states is convoluted by the experimental resolution (given by $\pm 0.075 \times E_e$, where E_e is the electron energy in eV); it is superimposed on the exponentially decreasing continuum provided by the decomposition method to get the full simulated spectrum. The bands observed in the experimental spectrum are fairly well located in the simulated spectrum. However, whatever the set of populations used, no acceptable fit of the relative intensities between peaks could be achieved. A better fit is shown in Fig. 9(a). It assumes an additional broad Gaussian peak centered at 0.45 eV with a FWHM of 0.18 eV. Although not perfect, this fit, the one obtained with the minimal assumptions listed above, reproduces the location and intensity of the main features of the experimental spectrum. The population of the electronic states of free barium used in the fit is shown in Fig. 9(b). The observed 495 K kinetic energy distribution of the ejected Ba and the fact discussed previously that it moves out of the cluster along repulsive curves may explain that no BaAr$_i^+$ (i small) are observed.

We are then left with the observation that only a fraction of the photoelectron signal can be assigned to free barium atoms, ejected out of the cluster. The simplest assumption concerning the remaining photoelectron signal, i.e., the exponentially decreasing continuum and the additional broad Gaussian peak, is to assign it to excited barium atoms staying on the cluster at long delay times. The existence of such a component is surprising at a first glance since the ejected barium atoms have lost $\sim$1.6 eV according to Fig. 9(b), hence suggesting that such a large energy release could make the probability of ejection close to unity. However, the examination of the velocity distribution of barium in Fig. 7 reveals that only 0.064 eV (corresponding to the 495 K Maxwellian velocity distribution) shows up as kinetic energy of
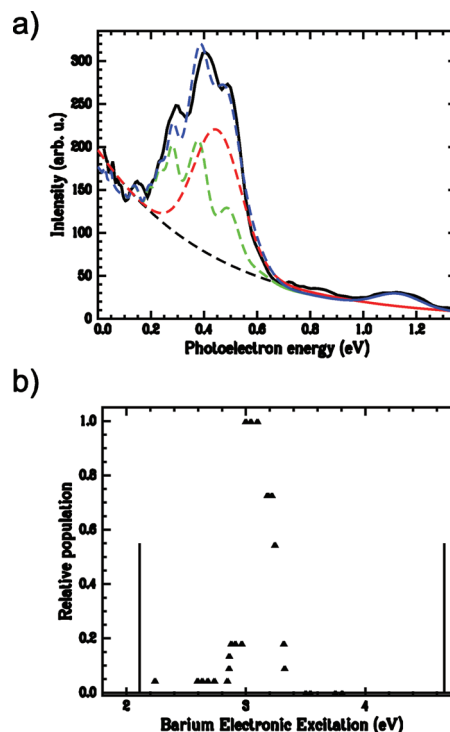

FIG. 9. (a) Simulated photoelectron spectrum (blue dashed curve) and experimental photoelectron spectrum of Fig. 5 (solid black curve). The dashed red and green curves are the components of the simulation, superimposed on the exponentially decreasing continuum. The dashed red curve is the Gaussian peak added to the simulation (center: 0.45 eV; FWHM: 0.18 eV), the green curve is the simulated photoelectron spectrum of free barium, assuming the relative populations given in (b). The vertical bar on the right is the excitation energy provided by the pump laser. That on the left is the energy limit of two-photon ionization at 792 nm.

the ejected barium. This is an indication that barium interacts strongly with the cluster during the chain of events, which leads to the final ejection of barium. This makes burying situations of low lying states of barium quite competing with ejections situation. The suggestion that such a competition exists is strengthened when considering that the ejection of barium is a very indirect and slow process, which can be observed up to 60 ps after the pump pulse (see the probability density function f describing the detection of Ba$^+$ ions in Fig. 6).

E. Electronic energy distribution of barium prior to its ejection from the cluster

The photoelectron spectrum, which appears in Fig. 4 at delay times $t < 5$ ps, informs on the time evolution of the electronic energy distribution of barium prior the ejection out of the cluster. Its full interpretation would go through a complete treatment of the movement of the initial wavepacket within the manifold of electronic states. This is beyond the scope of the present work. Here, likely directions are deduced from the experimental observations. Three broad photoelectron bands centered at 1.18, 0.59, and 0.46 eV are observed at time $t = 0$. They were assigned in Sec. VI A to the ionization by a single 792 nm photon of the initial Ba-cluster state, to Ba$^+(6s\ ^2S_{1/2})$, Ba$^+(5d\ ^2D_{3/2})$, and Ba$^+(5d\ ^2D_{5/2})$, respectively.

Section VI B suggested that the early dynamics following excitation by pump pulse corresponds to a progressive embedding of barium into argon. Assuming that the picture brought in Fig. 8 for the Ba–Ar diatomics is still valid for the $BaAr_{\approx 750}$ clusters, the embedding lowers both the ion energy and that of the neutral Rydberg states, with, however, a larger lowering for the ion due to the absence of electron screening. As long as no nonadiabatic energy transfer occurs, a shift of the photoelectron bands to larger energies is expected. This is actually observed in Fig. 4 since the photoelectron band at 1.18 eV shifts to 1.21 eV during the first 0.5 ps of the evolution. The prolate shape of the broad and intense massif overlapping the 0.59 and 0.46 eV photoelectron bands can be attributed to the same effect also.

In Sec. VI C we made the hypothesis that during the embedding process of barium into argon, a series of nonadiabatic energy transfers is at play, which lowers the barium electronic energy and eventually transfers a fraction of the barium atoms to repulsive potential energy surfaces. During this regime, the decreasing electronic energy of barium correlatively increases the vertical ionization energy and the kinetic energy of the photoelectron, which tracks this evolution, is expected to shift to lower energies. Apparently, this effect is observed in Fig. 4 when considering the electron band at 1.18 eV. After its energy has increased up to 1.21 eV (see interpretation above), it moves down to 0.93 eV when the delay times goes up to 2.9 ps. Hereafter, we call this band the *downshifting band*. Accordingly, its energy downshift from 1.21 to 0.93 eV would correspond to a lowering of the barium electronic energy from the initial $6s9p\ ^1P$ energy down to $6s7d\ ^3D$, across a series of 37 states, singlet and triplets belonging to the $5d6d$, $5d7p$, $6s5f$, $6s8d$, $6s9s$, $6s8p$, and $6s7d$ electronic configurations. Three considerations force to question this simple interpretation.

First, it is surprising that the downshifting effect is not observed on the photoelectron bands near 0.5 eV, which corresponds to the $Ba(5d6d\ ^1D) \rightarrow Ba^+(5d\ ^2D_{3/2,5/2})$ ionization. Second, the bands near 0.5 eV disappear very rapidly, although the discussion in the above paragraph suggests that states with $5d$ orbital in their electronic configuration are visited. Such states should indeed be ionized preferentially to $Ba^+(5d)$ and yield photoelectrons in the 0.5 eV range or below. Finally, the downshifting band vanishes after 3 ps, although the $Ba(6s9p\ ^1P) \rightarrow Ba^+(6s\ ^2S)$ ionization by a single 792 nm photon is still energetically possible. An alternative interpretation is considered now.

We discussed in Sec. VI A that after excitation by the pump laser, barium is likely to be in a coherent superposition of states with mixed electronic configurations, which include at least $6s9p$, $6s5f$, and $5d6d$. In the Ba–Ar diatomics the molecular states corresponding asymptotically to the $6s9p$, $6s5f$, and $5d6d$ configurations have an almost parallel behavior as the Ba–Ar distance is varied (see top panel in Fig. 8). The situation is likely different in the cluster since the size of the orbitals associated with the $6s9p$, $6s5f$, and $5d6d$ configurations is very different. Hence, the states, which are populated coherently by the pump laser, may behave differently in the cluster and the initial coherence may be lost as

the barium dynamics proceeds. Two behaviors may be thought of. One, characterizing the Rydberg $6s9p$ configuration, would account for *downshifting band*. Its energy downshift may reflect a progressive embedding and stabilization of the $Ba(6s)^+$ core within the cluster, accompanied by the promotion of the Rydberg electron to a diffuse orbital about the whole cluster. This promotion is likely to induce progressive loss of the oscillator strength for ionization by the probe laser, hence accounting for the observation that the *downshifting band* vanishes after ~ 3 ps. This situation is akin to that discussed in Ref. 47–50, where high Rydberg states are stabilized in rare gas matrices. The other behavior is linked to the $5d6d$ or $6s5f$ configurations, which have a less pronounced Rydberg character than $6s9p$, but which are involved in substantially attractive barium-cluster states. Efficient couplings between these states may be though of as with the network of predissociative states for these states. A rapid electronic relaxation is then expected in competition with predissociation.

VII. SUMMARY, DYNAMICAL MODEL, AND CONCLUSION

$Ba(Ar)_{\approx 750}$ clusters were generated by associating the supersonic expansion and the pick-up techniques. A femtosecond pump-probe experiment was performed. A laser at 266.3 nm, the pump, was used to excite barium within the cluster environment, and the resulting dynamics was followed by probing the system by ionization either at 792 nm (essentially) or 399.2 nm. This corresponds to probing the dynamics of a highly electronically excited barium atom within the multidimensional environment of an argon cluster. The velocity imaging technique was used to monitor the photoelectrons and photoions produced by the probe ionization as a function of the delay time between the pump and probe pulses. This provided a very complete set of data, which document the time evolution of the energy and angular distribution of the photoelectrons and photoions. Here, only the energy distributions of the photoions and photoelectrons were examined.

A complex dynamics was revealed, which likely involves a sequence/superposition of elementary processes, one of which is the ejection of barium out of the cluster. The latter has an efficiency, which starts increasing 5 ps after the pump pulse, the maximum ejection probability being at 10 ps. The ejection process lasts at a very long time, up to 60 ps. A competing process is the partial solvation of barium in low lying electronic states. Both processes are preceded by a complex electronic relaxation, which is not fully unraveled here.

Based on the Ba–Ar, Ba^+–Ar potential curves, together with simple additive considerations, the presumed dynamical picture that emerged from the discussion is the following. The pump laser creates a wavepacket corresponding to the superposition of a few electron configurations, the dominant one being $6s9p$, mixed with $5d6d$ and $6s5f$. This likely corresponds to a coherent superposition of several multiconfigurational states. The excitation turns on dynamics, which are dominated first by movements along attractive potential en-

ergy surfaces, resulting in a progressive embedding of barium into argon. Although the embedding is fairly certain, a question, which could not be answered here, is how deep excited barium is buried inside the cluster.

During this evolution, two different behaviors seem to be at play. One, associated with the $6s9p$ configuration, would be a fairly slow evolution, in ~ 3 ps toward the solvation of Ba$(6s)^+$ within the cluster and the excited electron moving in a perturbed diffuse orbital about the cluster. The other behavior, associated with the more compact $5d6d$ and $6s5f$ configurations, would result from an efficient network of couplings, which stimulate a fast relaxation of the electronic energy and a branching to the ejection of barium out of the cluster. The ejection process appears as undirect, converting a significant part of the released electronic energy into the cluster vibrational degrees of freedom. About 1.6 eV is released from the initial 4.66 eV electronic energy provided by the pump laser and only 0.064 eV shows up as kinetic energy of the ejected barium. Finally, a significant fraction of the barium atoms is not ejected out of the cluster. A component of the photoelectron was observed indeed at a large time delay, attributed to excited barium, which stays solvated in the cluster. Other channels certainly exist, where barium is relaxed to states, which are not detectable in the present experiment, e.g., electronic states below $6s6p$ ^1P.

The present work is a first step toward the detailed understanding of multidimensional dynamics, where the electronic degrees of freedom of a chromophore are coupled by the fluctuating interaction with numerous external degrees of freedom of a solvating environment. We have identified essential features but several questions are left opened and assumptions of the dynamical picture need to be substantiated by theoretical investigations and further experimental works. Of special relevance will be to document the loss of coherence of the wavepacket at early time delays, the interaction of Rydberg levels with a cluster, whose size is comparable to that of the Rydberg orbital. Moreover, full nonadiabatic simulations would be helpful to know which solvation configurations of barium result in trapping, which one leads to dissociative pathways, and what is the efficiency and the time scale for switching from trapping to ejection. A last issue is the role of autoionization, which has not been invoked yet. The high Rydberg states, which are initially populated in a cluster, are presumably less attractive than the ground state of the ionized system because the ion core of the Rydberg state is partially screened by the electron. Hence, it cannot be excluded that during the initial embedding step, the coupling with lower neutral states is in competition with autoionization. In addition to these theoretical investigations, running experiments at different pump wavelengths and recording photoelectron spectra with a better resolution is planned also to better document the branching ratio between the ejected and the solvated barium atoms and to examine how this ratio is affected by changes in the initial wavepacket.

ACKNOWLEDGMENTS

[1] L. Landau, Phys. Z. Sowjetunion **2**, 46 (1932).

[2] C. Zener, Proc. R. Soc. London, Ser. A **137**, 696 (1932).

[3] M. Bixon and J. Jortner, J. Chem. Phys. **48**, 715 (1968).

[4] P. M. Dinh, P. G. Reinhard, and E. Suraud, Phys. Rep. **485**, 43 (2010).

[5] J. C. Tully, J. Chem. Phys. **93**, 1061 (1990).

[6] F. Calvo, D. Bonhommeau, and P. Parneix, Phys. Rev. Lett. **99**, 083401 (2007).

[7] J. M. Mestdagh, M. A. Gaveau, C. Gée, O. Sublemontier, and J. P. Visticot, Int. Rev. Phys. Chem. **16**, 215 (1997).

[8] J. P. Visticot, J. Berlande, J. Cuvellier, A. Lallement, J. M. Mestdagh, P. Meynadier, P. d. Pujo, and O. Sublemontier, Chem. Phys. Lett. **191**, 107 (1992).

[9] P. d. Pujo, J. M. Mestdagh, J. P. Visticot, J. Cuvellier, P. Meynadier, O. Sublemontier, A. Lallement, and J. Berlande, Z. Phys. D: At., Mol. Clusters **25**, 357 (1993).

[10] B. Schilling, M. A. Gaveau, O. Sublemontier, J. M. Mestdagh, J. P. Visticot, X. Biquard, and J. Berlande, J. Chem. Phys. **101**, 5772 (1994).

[11] M. A. Gaveau, M. Briant, P. R. Fournier, J. M. Mestdagh, J. P. Visticot, F. Calvo, S. Baudrand, and F. Spiegelman, Eur. Phys. J. D **21**, 153 (2002).

[12] A. I. Krylov, R. B. Gerber, M. A. Gaveau, J. M. Mestdagh, B. Schilling, and J. P. Visticot, J. Chem. Phys. **104**, 3651 (1996).

[13] J. Nagl, A. W. Hauser, G. Aubock, C. Callegari, and W. E. Ernst, J. Phys. Chem. A **111**, 12386 (2007).

[14] F. Stienkemeier and K. K. Lehmann, J. Phys. B **39**, R127 (2006).

[15] B. Saha, R. Fukuda, H. Nakatsuji, and P. K. Mukherjee, Theor. Chem. Acc. **118**, 437 (2007).

[16] A. B. Pacheco, B. Thorndyke, A. Reyes, and D. A. Micha, J. Chem. Phys. **127**, 244504 (2007).

[17] Y. Ren and V. V. Kresin, Phys. Rev. A **76**, 043204 (2007).

[18] J. Nagl, G. Aubock, C. Callegari, and W. E. Ernst, Phys. Rev. Lett. **98**, 075301 (2007).

[19] J. Anton, P. K. Mukherjee, B. Fricke, and S. Fritzsche, J. Phys. B **40**, 2453 (2007).

[20] M. Leino, A. Viel, and R. E. Zillich, J. Chem. Phys. **129**, 184308 (2008).

[21] G. Aubock, J. Nagl, C. Callegari, and W. E. Ernst, Phys. Rev. Lett. **101**, 035301 (2008).

[22] P. Jungwirth and R. B. Gerber, J. Chem. Phys. **104**, 5803 (1996).

[23] M. C. Heitz, L. Teixidor, N. T. Van-Oanh, and F. Spiegelman, J. Phys. Chem. A **114**, 3287 (2010).

[24] R. Baumfalk, N. H. Nahler, U. Buck, M. Y. Niv, and R. B. Gerber, J. Chem. Phys. **113**, 329 (2000).

[25] N. H. Nahler, M. Farnik, U. Buck, H. Vach, and R. B. Gerber, J. Chem. Phys. **121**, 1293 (2004).

[26] J. Faeder and R. Parson, J. Chem. Phys. **108**, 3909 (1998).

[27] J. Douady, E. Jacquet, E. Giglio, D. Zanuttini, and B. Gervais, Chem. Phys. Lett. **476**, 163 (2009).

[28] L. Poisson, K. D. Raffael, B. Soep, J. M. Mestdagh, and G. Buntinx, J. Am. Chem. Soc. **128**, 3169 (2006).

[29] L. Poisson, K. D. Raffael, M. A. Gaveau, B. Soep, J. M. Mestdagh, J. Caillat, R. Taieb, and A. Maquet, Phys. Rev. Lett. **99**, 103401 (2007).

[30] J. Farges, M. F. d. Feraudy, B. Raoult, and G. Torchet, J. Chem. Phys. **84**, 3491 (1986).

[31] A. Eppink and D. H. Parker, Rev. Sci. Instrum. **68**, 3477 (1997).

[32] G. A. Garcia, L. Nahon, and I. Powis, Rev. Sci. Instrum. **75**, 4989 (2004).

[33] V. Mazet, "Développement de méthodes de traitement de signaux spectroscopiques: Estimation de la ligne de base et du spectre de raies," Ph.D. thesis, Nancy University, 2005.

[34] P. Liu, Q. Shi, H. Daume, and G. A. Voth, J. Chem. Phys. **129**, 214114 (2008).

[35] C. Robert, *The Bayesian Choice* (Springer-Verlag, Berlin, 2001).

[36] P. Green, Biometrika **82**, 711 (1995).

[37] S. Gulam Razul, W. Fitzgerald, and C. Andrieu, Nucl. Instrum. Methods Phys. Res. A **497**, 492 (2003).

[38] C. Robert and G. Casella, *Monte Carlo Statistical Methods* (Springer-Verlag, Berlin, 2002). http://cg.scs.carleton.ca/~luc/rnbookindex.html.

[39] E. Czuchaj, F. Rebentrost, H. Stoll, and H. Preuss, Theor. Chem. Acc. **100**, 117 (1998).

[40] A. Masson, M.-C. Heitz, and F. Spiegelman (in preparation).

[41] B. Huron, J. P. Malrieu, and P. Rancurel, J. Chem. Phys. **58**, 5745 (1973).

[42] S. Evangelisti, J. P. Daudey, and J. P. Malrieu, Chem. Phys. **75**, 91 (1983).

[43] F. Spiegelman, L. Maron, W. H. Breckenridge, J. M. Mestdagh, and J. P. Visticot, J. Chem. Phys. **117**, 7534 (2002).

[44] NIST-ASD Team, NIST Atomic Spectra Database (version 3) [online], available at http://www.nist.gov/physlab/data/asd.cfm (National Institute of Standards and Technology, Gaithersburg, MD, 2008).

[45] M. Aymar, C. H. Greene, and E. LucKoenig, Rev. Mod. Phys. **68**, 1015 (1996).

[46] C. E. Moore, *Atomic Energy Levels*, Natl. Bur. Stand. (U.S.) Circ. No. 467 (U.S. Department of Commerce, Washington, DC, 1958), Vol. III.

[47] M. Groß and F. Spiegelmann, J. Chem. Phys. **108**, 4148 (1998).

[48] M. Groß and F. Spiegelmann, Eur. Phys. J. D **4**, 219 (1998).

[49] F. Spiegelman, G. Durand, and M. C. Heitz, in *Condensed Matter Theory*, edited by M. Belkacem and M. Dinh (Nova Sciences, New York, 2005), Vol. 19.

[50] F. Vigliotti and M. Chergui, Eur. Phys. J. D **10**, 379 (2000).

[51] M. Ben El Hadj Rhouma, Z. Ben Lakhdar, H. Berriche, and F. Spiegelman, J. Chem. Phys. **125**, 084315 (2006).

[52] D. J. Wales and J. P. K. Doyle, J. Phys. Chem. A **101**, 5111 (1997).

[53] R. A. Aziz and H. H. Chen, J. Chem. Phys. **67**, 5719 (1977).

[54] V. S. Lebedev and I. L. Beigman, *Physics of Highly Excited Atoms and Ions* (Springer, New York, 1998).